Inorganic Chemistry

Article

Cite This: *Inorg. Chem.* 2018, 57, 12509−12520

pubs.acs.org/IC

First Dimethyltin-Functionalized Rare-Earth Incorporated Tellurotungstates Consisting of {B-α-TeW_7O_{28}} and {W_5O_{18}} Mixed Building Units

Jing-Lin Liu, Meng-Tian Jin, Li-Juan Chen,* and Jun-Wei Zhao*

Henan Key Laboratory of Polyoxometalate Chemistry, Institute of Molecule and Crystal Engineering, College of Chemistry and Chemical Engineering, Henan University, Kaifeng, Henan 475004, PR China

Supporting Information

ABSTRACT: The facile one-step assembly reaction of $Na_2WO_4{\cdot}2H_2O$, Sn-$(CH_3)_2Cl_2$, $RE(NO_3)_3{\cdot}6H_2O$ and K_2TeO_3 in the presence of dimethylamine hydrochloride as an organic solubilizing agent in acidic aqueous solution resulted in a family of dimethyltin-functionalized rare-earth (RE) incorporated tellurotungstates consisting of {B-α-TeW_7O_{28}} and {W_5O_{18}} mixed building units $[H_2N(CH_3)_2]_8Na_4H_2[RE_2(OH)(B\text{-}\alpha\text{-}TeW_7O_{28})Sn_2(CH_3)_4(W_5O_{18})]_2{\cdot}18H_2O$ [RE = Er^{III} (**1**), Yb^{III} (**2**), Ho^{III} (**3**), Y^{III} (**4**)]. The most striking structural characteristic of **1**−**4** is that they all contain a novel tetrameric *S*-shaped $[RE_2(OH)(B\text{-}\alpha\text{-}TeW_7O_{28})Sn_2(CH_3)_4(W_5O_{18})]_2^{14-}$ moiety simultaneously including two pentavacant Keggin $[B\text{-}\alpha\text{-}TeW_7O_{28}]^{12-}$ and two monovacant Lindqvist $[W_5O_{18}]^{6-}$ fragments connected by RE and dimethyltin linkers. To the best of our knowledge, such dimethyltin-functionalized RE-containing tellurotungstates have not been reported before. The visible or NIR solid-state emission spectra of **1** and **3** display the characteristic emission bands arising from Er^{III} and Ho^{III} centers. Moreover, various **1-Er/Yb** co-doped samples were prepared by controlling different mass ratio of $Er(NO_3)_3{\cdot}6H_2O/Yb(NO_3)_3{\cdot}6H_2O$ in the range of 0.96:0.04−0.02:0.98. In the visible region, the emission intensity of the **1-$Er_{0.40}$/$Yb_{0.60}$** co-doped sample reaches the maximum at the mass ratio of $Er(NO_3)_3{\cdot}6H_2O/Yb(NO_3)_3{\cdot}6H_2O$ being 0.40:0.60, and this observation is mainly derived from the fact that the Yb^{3+} ions can sensitize the Er^{3+} ions to enhance the emission intensity in the visible region. However, no such phenomenon for the **1-Er/Yb** co-doped samples is seen in the NIR region. Besides, the upconversion spectra of the **1-Er/Yb** co-doped samples were first observed. In addition, the thermal stabilities of **1**−**4** were also investigated on the crystalline samples and the thermal decomposition process of **1** has been deeply studied.

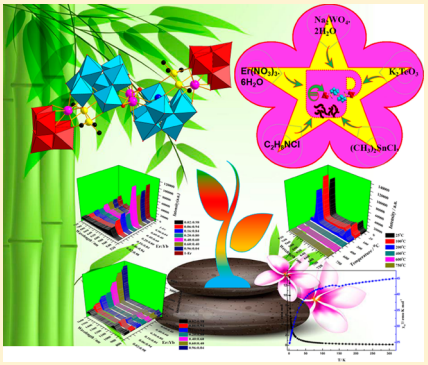

INTRODUCTION

Polyoxometalates (POMs) are an outstanding class of metal−oxygen cluster compounds, which exhibit compositional diversity and structural variety as well as a wide range of application prospects in catalysis, magnetism, medicine, material science, optics, biology, and nanotechnology.[1−6] It is noteworthy that tellurotungstates (TTs), as an important subset of POM chemistry, have attracted increasing interest in the past several decades. Since Nerevyatkina et al. first communicated the Anderson-type TT-based polyoxoanion $[TeW_6O_{24}]^{6-}$ in 1965,[7] some novel TT derivatives were continuously discovered. In 2003, Pope et al. addressed an unique diuranyl substituted sandwich-type species $[(UO_2)_2(H_2O)_2(TeW_9O_{33})_2]^{12-}$.[8] In 2011, Cronin and co-workers prepared several innovative macrocyclic nanoscale poly(TT) aggregates $[W_{28}Te_8O_{112}]^{24-}$, $[W_{28}Te_9O_{115}]^{26-}$ and $[W_{28}Te_{10}O_{118}]^{28-}$, where the tellurite anions can act as templates within structural building units and linkers between them as well as pendant ligands in control of intercluster aggregation.[9]

Recently, great research efforts have been paid to designing and synthesizing POM-based materials by using TTs as building blocks. To date, remarkable achievements have been made in transition-metal (TM) substituted TTs such as $[(Mn^{II}(H_2O)_3)_2(Mn^{II}(H_2O)_2)_2(TeW_9O_{33})_2]^{8-}$,[10] $[Fe_4(H_2O)_{10}(\beta\text{-}TeW_9O_{33})_2]^{4-}$,[11] $[\{Ru^{IV}{}_4O_6(H_2O)_9\}_2\{Fe(H_2O)_2\}_2\{\beta\text{-}TeW_9O_{33}\}_2H]^{-}$,[12] $[H_{10}Ag_{18}Cl(Te_3W_{38}O_{134})_2]^{29-}$,[13] $[Pd_6Te_{19}W_{42}O_{190}]^{40-}$,[14] and $[\{Co(L)(H_2O)\}_2(WO_2)_2(TeW_9O_{33})_2]^{10-}$ (L = 1H-imidazole-4-carboxylate).[15] In contrast, relevant reports on RE-substituted TTs (RESTTs) are rather rare except that two unseen nanosized octameric multi-Ce-containing TT aggregates $[\{(TeO_3)W_{10}O_{34}\}_8\{Ce_8(H_2O)_{20}\}(WO_2)_4(W_4O_{12})]^{48-}$ and $[Ce_{10}Te_8W_{88}O_{298}(OH)_{12}(H_2O)_{40}]^{18-}$ were reported by Su and co-workers[16,17] and a family of novel organic−inorganic hybrid tetrameric RESTTs $[RE_2(H_2O)_4(pica)_2W_2O_5][(RE(H_2O)W_2(Hpica)_2O_4)(B\text{-}\beta\text{-}TeW_8O_{30}H_2)_2]_2^{4-}$ (RE = La^{III}, Ce^{III}, Nd^{III}, Sm^{III}, Eu^{III}; Hpica = 2-picolinic acid) were discovered by our group.[18] In addition, the organometal functionalized TTs have been developed as an important research focus and a challeneable area because organometal

Received: May 30, 2018
Published: October 3, 2018

DOI: 10.1021/acs.inorgchem.8b01486
Inorg. Chem. 2018, 57, 12509−12520

compounds demonstrate potential applications in diverse fields such as catalysis, nonlinear optics, medicine, and so on.[19−21] For instance, in 2015, Niu and collaborators addressed a trivacant Keggin TT-based carbonyl manganese derivative $[\{Mn(CO)_3\}(Mn(H_2O)_2)(Mn(H_2O)_3)(TeW_9O_{33})]_2^{6-}$.[22] In 2016, Bi et al. prepared an organoruthenium substituted TT $[Te_2W_{20}O_{70}(RuC_6H_6)_2]^{8-}$ and evaluated its catalytic activity toward the aerobic oxidation of n-tetradecane when it was anchored on 3-aminopropyltriethoxysilane-modified SBA-15.[23] Among various organometals, organotin species have aroused gigantic interest in POM field due to the stability of the Sn−C bond in aqueous media and the appropriate size of Sn^{IV} to occupy addenda sites in POM skeletons.[24]

However, intensive investigations on organotin and RE co-embedded heterometallic TTs are underdeveloped, which provides us for an excellent opportunity. Recently, with the aim of discovering novel organotin and RE coembedded heterometallic TTs, our group have launched systematic explorations on this system and obtained a group of unprecedented TT-based organotin−RE heterometallic hybrids with four organic components $[H_2N(CH_3)_2]_6H_{12}Na_2\{[Sn(CH_3)W_2O_4(IN)]\ [(B\text{-}\alpha\text{-}TeW_8O_{31})RE(H_2O)(Ac)]_2\}_2\cdot 25H_2O$ (RE = Ce^{III}, Pr^{III}, Nd^{III}, Sm^{III}, Eu^{III}, Gd^{III}, Tb^{III}).[25] As a part of our ongoing work, we proceeded to explore this system to find innovative TT-based organotin−RE heterometallic hybrids containing mixed POM building units by the one-pot self-assembly strategy based on the following ideas: (a) According to our recent studies on the lone-electron-pair trigonal- pyramidal-As/Se/TeO_3 inducing syntheses of multi-RE encapsulated heteropolyoxotungstates by the one-pot self-assembly strategy,[18,25−28] it is found that arsenotungstate and selenotungstate easily form trivacant Keggin POM fragments, whereas TT tends to generate tetravacant Keggin POM fragments. In comparison with the As^{III} and Se^{IV} atoms, the Te^{IV} atom has the larger atomic radius and the lone-electron pair located on the trigonal-pyramidal-TeO_3 group can shows the obvious stereochemical effect, so it is believed that TT can create much higher vacant TT fragment if reaction conditions are suitable. (b) In the reaction system, increasing the amount of Na_2WO_4 may produce isopolyoxotungstate fragments as well as multivacant TT fragments, which will favor to construct novel TT-based organotin − RE heterometallic hybrids containing mixed POM building units. (c) The synergistic interactions between the appropriate size of Sn^{IV} to occupy addenda sites in POM skeletons and the high coordination requirements and the strong oxophilicity of RE electrophiles can synchronously stabilize in situ formed multivacant TT fragments and isopolyoxotungstate fragments. Moreover, organotin groups and RE cations can function as excellent connectors to link different POM building units together, giving rise to multicomponent ploy(POM) aggregates with unexpected structures and fascinating properties. In addition, dimethylamine hydrochloride can act as an organic solubilizer to effectively improve the reactivity between in situ formed TT fragments and RE cations in aqueous medium, and protonated dimethylamine cations can serve as the counter cations to balance the charge of ploy(POM) anions and further consolidate the structures of ploy(POM) aggregates. Through a great deal of our efrt, a family of unique dimethyltin−RE incorporated TTs consisting of {B-α- TeW_7O_{28}} and {W_5O_{18}} mixed building units $[H_2N(CH_3)_2]_8Na_4H_2$ $[RE_2(OH)(B\text{-}\alpha\text{-}TeW_7O_{28})Sn_2(CH_3)_4(W_5O_{18})]_2\cdot 18H_2O$ [RE = Er^{III} (**1**), Yb^{III} (**2**), Ho^{III} (**3**), Y^{III} (**4**)] have been successfully obtained by the one-pot assembly reaction of $Na_2WO_4\cdot 2H_2O$, $RE(NO_3)_3\cdot 6H_2O$, K_2TeO_3, $Sn(CH_3)_2Cl_2$, and dimethylamine hydrochloride under bench conditions. Besides, they have also been characterized by elemental analyses, IR spectroscopy, powder X-ray diffraction (PXRD), thermogravimetric (TG) analysis, and single-crystal X-ray diffraction. The thermal stability of **1** has been investigated at great length by variable-temperature IR spectra, variable-temperature PXRD patterns, and variable-temperature luminescence measurements. Besides, the solid-state luminescent measurements of **1** and **3** show that their emission spectra display the characteristic emission bands arising from Er^{III} and Ho^{III} centers, respectively. Moreover, various **1-Er/Yb** co-doped samples were synthesized and their emission spectra in the visible and NIR regions were also collected under the excitation at 381 nm. The UC emission behavior of **1-Er/Yb** co-doped samples was observed upon the excitation at 980 nm at room temperature. In addition the magnetic susceptibility properties of **1** have been studied in the temperature range of 2−300 K.

EXPERIMENTAL SECTION

Materials and Methods. All chemical reagents are at least analytical grade and used without further purification. C, H and N elemental analyses were measured on a Perkin−Elmer 2400-II CHNS/O analyzer. Inductively coupled plasma atomic emission spectrometry (ICP−AES) was performed with a Perkin−Elmer Optima 2000 ICP−AES spectrometer. PXRD patterns were collected on a Bruker AXS D8 Advance diffractometer instrument with Cu Kα radiation (λ = 1.54056 Å) at 293 K. IR spectra were recorded from solid samples palletized with KBr on a Nicolet 170 SXFT−IR spectrometer in the range of 4000−400 cm^{-1}. TG analyses were obtained under N_2 atmosphere using a Mettler Toledo TGA/SDTA 851^e instrument with a heating rate of 10 °C min^{-1} from 25 to 800 °C. Photoluminescence (PL) and lifetime spectra were recorded on an FLS 980 Edinburgh Analytical Instrument apparatus equipped with a 450 W xenon lamp and a μF900H high-energy microsecond flash lamp as the excitation source at room temperature. Variable-temperature magnetic measurements were conducted on the Quantum Design SQUID magnetometer (MPMS−VSM) in the range of 2−300 K.

Synthesis of $[H_2N(CH_3)_2]_8Na_4H_2[Er(OH)(B\text{-}\alpha\text{-}TeW_7O_{28})ErSn_2(CH_3)_4(W_5O_{18})]_2\cdot 18H_2O$ (1). $Na_2WO_4\cdot 2H_2O$ (3.500 g, 10.612 mmol), K_2TeO_3 (0.200 g, 0.7839 mmol), $Sn(CH_3)_2Cl_2$ (0.220 g, 1.001 mmol), and dimethylamine hydrochloride (2.000 g, 24.445 mmol) were successively added to 30 mL water with vigorous stirring. The pH value of the clear solution was adjusted to 6.50 by 6 mol·L^{-1} HCl. The resulting solution was stirred for around 10 min. Then, $Er(NO_3)_3\cdot 6H_2O$ (0.500 g, 1.143 mmol) was added. The final pH value of the solution was kept at 6.50 by addition of 0.5 mol·L^{-1} HCl. After constant stirring for another 30 min, the solution was filtered. Slow evaporation of the filtrate at ambient temperature resulted in pink prism crystals of **1** after approximately 3 weeks. Yield: 0.905 g (28.56%) based on K_2TeO_3. Elemental analyses calcd (%) for **1**: C, 3.52; H, 1.58; N, 1.37; Na, 0.56; Sn, 5.81; Te, 3.12; Er, 8.18; W, 53.95. Found: C, 3.71; H, 1.72; N, 1.56; Na, 0.48; Sn, 5.65; Te, 3.27; Er, 8.00; W, 54.12.

Synthesis of $[H_2N(CH_3)_2]_8Na_4H_2[Yb(OH)(B\text{-}\alpha\text{-}TeW_7O_{28})YbSn_2(CH_3)_4(W_5O_{18})]_2\cdot 18H_2O$ (2). The synthetic procedure of **2** is similar to that of **1** except that $Er(NO_3)_3\cdot 6H_2O$ was replaced by $Yb(NO_3)_3\cdot 6H_2O$ (0.500 g, 1.113 mmol). The colorless prism crystals of **2** were obtained. Yield: 0.863 g (27.16%) based on K_2TeO_3. Elemental analysis calcd (%) for **2**: C, 3.51; H, 1.57; N, 1.37; Na, 0.56; Sn, 5.79; Te, 3.11; Yb, 8.44; W, 53.80. Found: C, 3.73; H, 1.79; N, 1.50; Na, 0.44; Sn, 5.61; Te, 3.30; Yb, 8.26; W, 54.07.

Synthesis of $[H_2N(CH_3)_2]_8Na_4H_2[Ho(OH)(B\text{-}\alpha\text{-}TeW_7O_{28})HoSn_2(CH_3)_4(W_5O_{18})]_2\cdot 18H_2O$ (3). The synthetic procedure of **3** is similar to that of **1** except that $Er(NO_3)_3\cdot 6H_2O$ was replaced by $Ho(NO_3)_3\cdot 6H_2O$ (0.500 g, 1.089 mmol). The yellowish prism

DOI: 10.1021/acs.inorgchem.8b01486
Inorg. Chem. 2018, 57, 12509−12520

Table 1. Crystallographic Data and Structure Refinements for 1−4

	1	2	3	4
empirical formula	$C_{24}H_{128}N_8Na_2O_{112}Sn_4$ $Te_2W_{24}Er_4$	$C_{24}H_{128}N_8Na_2O_{112}Sn_4$ $Te_2W_{24}Yb_4$	$C_{24}H_{128}N_8Na_2O_{112}Sn_4$ $Te_2W_{24}Ho_4$	$C_{24}H_{128}N_8Na_2O_{112}Sn_4$ $Te_2W_{24}Y_4$
FW	8178.56	8201.84	8169.40	7865.32
crystal system	monoclinic	monoclinic	monoclinic	monoclinic
space group	$P2/c$	$P2/n$	$P2/n$	$P2/n$
a, Å	17.923(3)	17.911(3)	17.9160(18)	17.9782(19)
b, Å	17.882(3)	17.910(3)	17.8728(19)	17.976(2)
c, Å	29.463(4)	24.979(4)	24.958(3)	25.055(3)
α, deg	90	90	90	90
β, deg	122.220(7)	94.938(3)	95.070(2)	95.025(2)
γ, deg	90	90	90	90
V, Å^{-3}	7989(2)	7983(2)	7960.4(14)	8065.8(15)
Z	2	2	2	2
μ, mm^{-1}	20.337	20.593	20.289	19.508
$F(000)$	7193	7212	7188	6964
T, K	296(2)	296(2)	296(2)	296(2)
limiting indices	$-19 \le h \le 21$ $-20 \le k \le 21$ $-34 \le l \le 34$	$-21 \le h \le 21$ $-18 \le k \le 21$ $-29 \le l \le 24$	$-18 \le h \le 21$ $-17 \le k \le 21$ $-29 \le l \le 29$	$-20 \le h \le 21$ $-19 \le k \le 21$ $-29 \le l \le 23$
no. of reflections collected	39604	39130	40254	40453
no. of independent reflections	13959	13937	13879	14161
R_{int}	0.1268	0.1135	0.1242	0.0776
data/restrains/parameters	13959/27/675	13937/57/668	13879/31/669	14161/0/666
goodness-of-fit on F^2	1.015	1.024	1.004	1.029
final R indices $[I > 2\sigma(I)]$	R_1 = 0.0786 wR_2 = 0.1484	R_1 = 0.0962 wR_2 = 0.2298	R_1 = 0.0641 wR_2 = 0.1121	R_1 = 0.0538 wR_2 = 0.1168
R indices (all data)	R_1 = 0.1526 wR_2 = 0.1671	R_1 = 0.1633 wR_2 = 0.2544	R_1 = 0.1417 wR_2 = 0.1279	R_1 = 0.1130 wR_2 = 0.1306

crystals of **3** were obtained. Yield: 0.883 g (27.89%) based on K_2TeO_3. Elemental analysis calcd (%) for **3**: C, 3.53; H, 1.58; N, 1.37; Na, 0.56; Sn, 5.81; Te, 3.12; Ho, 8.08; W, 54.01. Found: C, 3.76; H, 1.75; N, 1.45; Na, 0.49; Sn, 5.70; Te, 3.35; Ho, 7.92; W, 54.19.

Synthesis of $[H_2N(CH_3)_2]_8Na_4H_2[Y(OH)(B\text{-}\alpha\text{-}TeW_7O_{28})YSn_2(CH_3)_4(W_5O_{18})]_2\cdot 18H_2O$ (4). The synthetic procedure of **4** is similar to that of **1** except that $Er(NO_3)_3\cdot 6H_2O$ was replaced by $Y(NO_3)_3\cdot 6H_2O$ (0.500 g, 1.306 mmol). The colorless prism crystals of **4** were obtained. Yield: 0.763 g (25.06%) based on K_2TeO_3. Elemental analysis calcd (%) for **4**: C, 3.67; H, 1.64; N, 1.42; Na, 0.58; Sn, 6.04; Te, 3.24; Y, 4.52; W, 56.10. Found: C, 3.89; H, 1.81; N, 1.54; Na, 0.43; Sn, 5.90; Te, 3.31; Y, 4.33; W, 56.29.

Preparations of 1-Er/Yb Co-Doped Samples. The synthetic procedures of **1-Er/Yb** co-doped samples are similar to that of **1** except that $Er(NO_3)_3\cdot 6H_2O$ was replaced by the mixture of $Er(NO_3)_3\cdot 6H_2O$/$Yb(NO_3)\cdot 6H_2O$ with different mass ratios. Meanwhile, the total mass of $Er(NO_3)_3\cdot 6H_2O$ and $Yb(NO_3)\cdot 6H_2O$ still is set as 0.500 g. The different mass ratios of $Er(NO_3)_3\cdot 6H_2O$/$Yb(NO_3)\cdot 6H_2O$ are 0.02:0.98, 0.06:0.94, 0.16:0.84; 0.20:0.80, 0.40:0.60, 0.60:0.40, and 0.96:0.04. The resulting corresponding **1-Er/Yb** co-doped samples are named as **1-$Er_{0.02}$/$Yb_{0.98}$**, **1-$Er_{0.06}$/$Yb_{0.94}$**, **1-$Er_{0.16}$/$Yb_{0.84}$**, **1-$Er_{0.20}$/$Yb_{0.80}$**, **1-$Er_{0.40}$/$Yb_{0.60}$**, **1-$Er_{0.60}$/$Yb_{0.40}$** and **1-$Er_{0.96}$/$Yb_{0.04}$**. Elemental analysis calcd (%) for **1-$Er_{0.02}$/$Yb_{0.98}$**, Er, 0.16; Yb, 8.27. Found: Er, 0.24; Yb, 8.11. Elemental analysis calcd (%) for **1-$Er_{0.06}$/$Yb_{0.94}$**, Er, 0.49; Yb, 7.93. Found: Er, 0.38; Yb, 8.05. Elemental analysis calcd (%) for **1-$Er_{0.16}$/$Yb_{0.84}$**, Er, 1.31; Yb, 7.09. Found: Er, 1.16; Yb, 7.26. Elemental analysis calcd (%) for **1-$Er_{0.20}$/$Yb_{0.80}$**, Er, 1.63; Yb, 6.76. Found: Er, 1.79; Yb, 6.61. Elemental analysis calcd (%) for **1-$Er_{0.40}$/$Yb_{0.60}$**, Er, 3.27; Yb, 5.07. Found: Er, 3.14; Yb, 5.22. Elemental analysis calcd (%) for **1-$Er_{0.60}$/$Yb_{0.40}$**, Er, 4.90; Yb, 3.38. Found: Er, 5.08; Yb, 3.14. Elemental analysis calcd (%) for **1-$Er_{0.96}$/$Yb_{0.04}$**, Er, 7.85; Yb, 0.34. Found: Er, 8.01; Yb, 0.46.

X-ray Crystallography. A suitable good-quality single crystal for **1−4** was prudentially picked under an optical microscope and placed on a fine glass bar via glue. Single-crystal X-ray diffraction data of **1−4** were collected on a Bruker APEX−II CCD sealed tube diffractometer with graphite monochromated Mo Kα radiation (λ = 0.71073 Å) at 296(2) K. Their structures were determined through direct methods and consecutive full-matrix least-squares methods refined on F^2 using the SHELXTL−97 program package.[29,30] The remaining atoms were found from successive full-matrix least-squares refinements on F^2 and Fourier syntheses. Lorentz polarization and SADABS corrections were also applied.[31] No hydrogen atoms associated with water molecules were located from the difference Fourier map. All hydrogen atoms associated with carbon and nitrogen atoms were geometrically placed in calculated positions using a riding model and were refined isotropically using the default SHELXTL parameters. Non-hydrogen atoms were refined anisotropically. For **1−4**, there are still solvent-accessible voids in the check CIF reports of crystal structures, suggesting that some water molecules or organic cations should exist in the structures that cannot be found from the weak residual electron peaks. These water molecules are highly disordered, and attempts to locate and refine them were unsuccessful. On the basis of elemental analyses and TG analyses, another nine water molecules for **1** and nine water molecules and another two $[H_2N(CH_3)_2]^+$ cations for **2−4** were directly added to the molecular formula. Crystallographic data and structure refinements for **1−4** are demonstrated in Table 1.

RESULTS AND DISCUSSION

Structural Description. Bond valence sum (BVS) calculations for **1−4** indicate that the oxidation states of all W, RE, and Te centers are +6, +3, and +4, respectively (Table S1),[32] and a detailed summary of the bond lengths of each Ln ion in **1−4** are listed in Table S2.

X-ray single-crystal diffraction reveals that the molecular structures of **1−4** contain a novel tetrameric S-shaped

DOI: 10.1021/acs.inorgchem.8b01486
Inorg. Chem. 2018, 57, 12509−12520

dimethyltin-functionalized RE incorporated TT polyoxoanion $[RE_2(OH)(B\text{-}\alpha\text{-}TeW_7O_{28})Sn_2(CH_3)_4(W_5O_{18})]_2^{14-}$; therefore, only the structure of **1** is described in detail as a representative. The molecular structure of **1** encompasses a dimethyltin-functionalized Er-incorporated tetrameric TT polyoxoanion $[Er(OH)(B\text{-}\alpha\text{-}TeW_7O_{28})ErSn_2(CH_3)_4(W_5O_{18})]_2^{14-}$ (**1a**) (Figure 1a), four Na^+ cations,

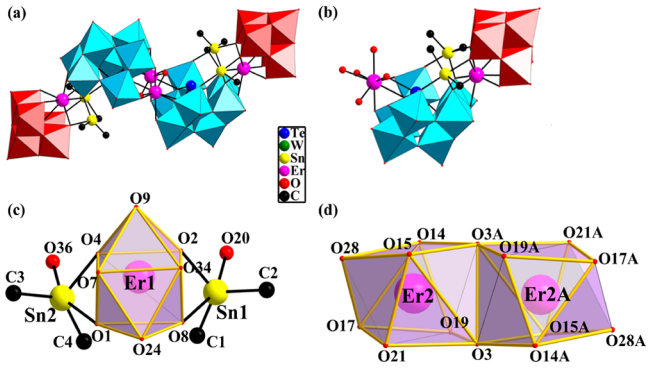

Figure 1. (a) Dimethyltin-functionalized Er-incorporated tetrameric polyoxoanion of **1**. (b) Dimeric unit $[Er(OH)(B\text{-}\alpha\text{-}TeW_7O_{28})ErSn_2(CH_3)_4(W_5O_{18})]^{7-}$ in **1a**. (c) Combination motif of $Sn1^{4+}$, $Er1^{3+}$ and $Sn2^{4+}$ centers. (d) Dinuclear $\{Er_2(OH)_2\}^{4+}$ cluster highlighting the severely distorted square antiprismatic geometry of the $Er2^{3+}$ ion. The atoms with the suffix A are generated by the symmetry operation where A: $-x, -y, -z$. Hydrogen atoms, protons, and lattice water molecules are omitted for clarity.

two protons, eight monoprotonated $[H_2N(CH_3)_2]^+$ cations, and 18 lattice water molecules. **1a** can be described as two equivalent dimeric units $[Er(OH)(B\text{-}\alpha\text{-}TeW_7O_{28})ErSn_2(CH_3)_4(W_5O_{18})]^{7-}$ (Figure 1b) linked by sharing a dinuclear $\{Er_2(OH)_2\}^{4+}$ cluster. In the dimeric unit, the crystallographically unique $Er1^{3+}$ cation binds to two μ_2-O atoms (O34, O7), two μ_3-O atoms (O1, O8), and one μ_6-O atom (O24) from the $[W_5O_{18}]^{6-}$ subunit as well as three μ_3-O atoms (O4, O2, O9) from the $[B\text{-}\alpha\text{-}TeW_7O_{28}]^{10-}$ subunit (Figure 1c), achieving an eight-coordinate severely distorted bicapped trigonal prism geometry, in which two bottom planes are occupied by the O2, O8, O34 group and the O1, O4, O7 group, respectively, whereas two cap positions are occupied by O9 and O24, respectively (Figure S1). The Er1−O bond lengths of 2.253(16)−2.658(15) Å and the O−Er1−O bond angles of 64.2(5)−152.6(5)° are basically within the normal range of the eight-coordinate Er^{3+} system. Whereas the $Er2^{3+}$ cation is located in the center of the eight-coordinate severely distorted square antiprismatic prism where two μ_2-O atoms (O21, O28) and one μ_4-O atom (O15) from one $[B\text{-}\alpha\text{-}TeW_7O_{28}]^{10-}$ subunit, two μ_2-OH atoms (O3, O3A) connecting $Er2^{3+}$ and $Er2A^{3+}$ cations, two μ_2-O atoms (O14, O17), and one μ_4-O atom (O19) from the other $[B\text{-}\alpha\text{-}TeW_7O_{28}]^{10-}$ subunit (Figure 1d). Besides, two bottom planes of the square prism are defined by the O3, O17, O19, O21 group and the O3A, O14, O15, O28 group, respectively (Figure S2). The Er2−O bond lengths of 2.270(16)−2.547(15) Å and the O−Er2−O bond angles of 66.8(5)−163.5(5)° are also accordance with the octa-coordinate Er^{3+} system. In addition, on both sides of the $Er1^{3+}$ cation, two crystallographically independent Sn^{4+} centers display the penta-coordinate highly distorted trigonal bipyramid geometry. The $Sn1^{4+}$ cation acts as a left-bridging moiety coordinated to three oxygen atoms from $[W_5O_{10}]^{6-}$ and $[B\text{-}\alpha\text{-}TeW_7O_{28}]^{10-}$ fragments (O2, O8, O20) and two methyl groups (C1, C2). In contrast to the $Sn1^{4+}$ cation, the $Sn2^{4+}$ cation acts as a right-bridging moiety binding to two O atoms (O4, O36) from $[B\text{-}\alpha\text{-}TeW_7O_{28}]^{10-}$ and the O1 atom from $[W_5O_{10}]^{6-}$ as well as two C3 and C4 atoms (Figure 1c). The existence of two Sn^{4+} cations further stabilize the open dimeric unit $[Er(OH)(B\text{-}\alpha\text{-}TeW_7O_{28})ErSn_2(CH_3)_4(W_5O_{18})]^{7-}$ by grafting to the vacant positions through three Sn−O bonds. The Sn−O bond lengths are in the range of 2.017(15)−2.237(16) Å (Figures S3 and S4).

One fascinating structural feature is that the $Er1^{3+}$ cation inserts the vacant site of the monovacant Lindqvist $[W_5O_{18}]^{6-}$ fragment through two μ_2-O atoms, two μ_3-O atoms, and one μ_6-O atom, forming a mono-Er-substituted Lindqvist $[ErW_5O_{18}]^{3-}$ fragment; meanwhile, two $[Sn(CH_3)_2]^{2+}$ cations graft to the $[ErW_5O_{18}]^{3-}$ fragment via two μ_3-O atoms, giving rise to an unprecedented mono-Er-inserted dimethyltin-decorated Lindqvist $[ErSn_2(CH_3)_4(W_5O_{18})]^+$ entity (Figure S5a). More intriguingly, $[ErSn_2(CH_3)_4(W_5O_{18})]^+$ and $[B\text{-}\alpha\text{-}TeW_7O_{28}]^{10-}$ (Figure S5b) groups are combined together, generating an unique dimeric $[(B\text{-}\alpha\text{-}TeW_7O_{28})ErSn_2(CH_3)_4(W_5O_{18})]^{9-}$ moiety (Figure S5c). Thus, **1a** (Figure S5e) can be also visualized to be constructed from two dimeric $[(B\text{-}\alpha\text{-}TeW_7O_{28})ErSn_2(CH_3)_4(W_5O_{18})]^{9-}$ moieties joined through a dinuclear $\{Er_2(OH)_2\}^{4+}$ cluster (Figure S5d). It should be pointed out that the pentavacant Keggin $[B\text{-}\alpha\text{-}TeW_7O_{28}]^{10-}$ fragment (Figure S6a) can be derived from the trivacant Keggin $[B\text{-}\alpha\text{-}TeW_9O_{33}]^{8-}$ fragment (Figure S6b) by the removal of two corner-sharing $\{WO_6\}$ octahedra (Figure S6c). From another perspective, **1a** (Figure 2a) can also be

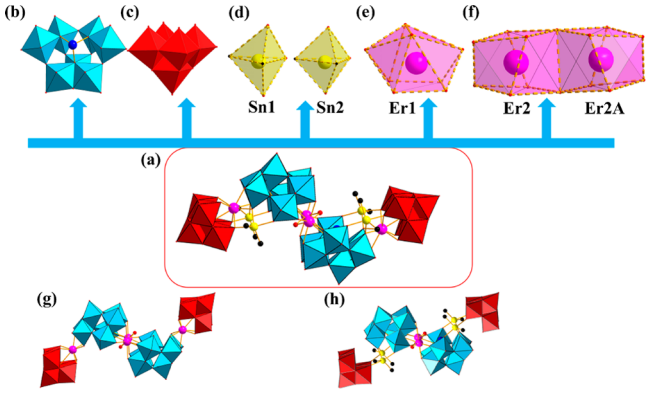

Figure 2. (a) View of **1a**. (b) Pentavacant Keggin $[B\text{-}\alpha\text{-}TeW_7O_{28}]^{10-}$ fragment. (c) Monovacant Lindqvist $[W_5O_{18}]^{6-}$ fragment. (d) Trigonal bipyramids of the $Sn1^{4+}$ and $Sn2^{4+}$ cations. (e) Bicapped trigonal prism of the $Er1^{3+}$ ion. (f, g) View of the $[Er(OH)(B\text{-}\alpha\text{-}TeW_7O_{28})Er(W_5O_{18})]_2^{22-}$ subunit. (h) View of the $[Er(OH)(B\text{-}\alpha\text{-}TeW_7O_{28})Sn_2(CH_3)_4(W_5O_{18})]_2^{20-}$ subunit.

visualized as a assembly of two pentavacant Keggin $[B\text{-}\alpha\text{-}TeW_7O_{28}]^{10-}$ fragments (Figure 2b), two monovacant Lindqvist $[W_5O_{18}]^{6-}$ fragments (Figure 2c), four $[Sn(CH_3)_2]^{2+}$ cations (Figure 2d), two $Er1^{3+}$ cations (Figure 2e), and a $\{Er_2(OH)_2\}^{4+}$ cluster (Figure 2f). In **1a**, the nonsymmetric sandwich-type $[(B\text{-}\alpha\text{-}TeW_7O_{28})ErSn_2(CH_3)_4(W_5O_{18})]^{9-}$ subunit (Figure S5c) is formed via a pentavacant Keggin $[B\text{-}\alpha\text{-}TeW_7O_{28}]^{10-}$ segment and a monovacant Lindqvist $[W_5O_{18}]^{6-}$ segment anchoring one $\{Sn_2(CH_3)_4Er\}$ cluster. As far as we know, such nonsymmetric

DOI: 10.1021/acs.inorgchem.8b01486
Inorg. Chem. 2018, 57, 12509−12520

sandwich-type $[(B\text{-}\alpha\text{-}TeW_7O_{28})ErSn_2(CH_3)_4(W_5O_{18})]^{9-}$ subunit is first observed in POM chemistry. When four $[Sn(CH_3)_2]^{2+}$ cations are removed away from **1a**, the tetrameric POM skeleton can be also retained (Figure 2g). However, in the absence of two $Er1^{3+}$ cations, the whole tetrameric POM framework is also maintained (Figure 2g).

Moreover, the 3D packing for **1a** is quite interesting. Viewed along the *c* axis, two neighboring layers (named layers A and B) are arranged in the −ABAB− pattern (Figure S7a,d). In the layer A, neighboring **1a** polyoxoanions are regularly aligned in the −AAA− mode toward the left orientation (Figure S7b,e). On the contrary, neighboring **1a** polyoxoanions in the layer B display the −AAA− mode toward the right orientation (Figure S7c,f). The 3D supramolecualr packing architecture of **1a** along the *a* axis is illustrated in Figure 3a, and neighboring **1a**

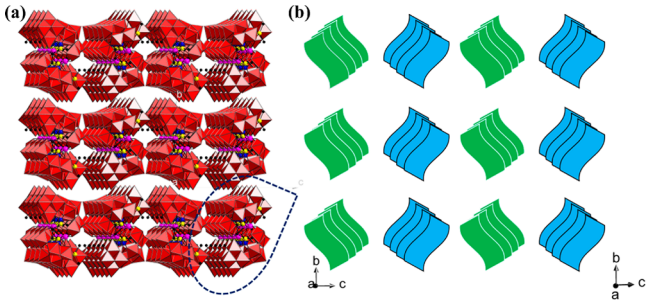

Figure 3. (a) 3D supramolecular packing of **1a** viewed along the *a* axis. (b) Simplified 3D supramolecular packing of **1a** viewed along the *a* axis.

polyoxoanions show −ABAB− mode in the *c* axis (Figure 3b). The distances between two adjacent **1a** polyoxoanions are 17.923 Å along the *a* axis, 17.882 Å along the *b* axis, and 29.463 Å along the *c* axis. The discrete monoprotonated $[H_2N(CH_3)_2]^+$ cations are distributed in the space formed by **1a** polyoxoanions and interact with some lattice water molecules and polyoxoanions by hydrogen bonding interactions with N−H···O distances of 2.64(8)−3.27(3) Å.

Thermogravimetric (TG) Analysis. The TG analyses of **1**−**4** were performed on pure crystalline samples in flowing N_2 atmosphere from 25 to 800 °C to examine their thermal stability (Figure S8), which show similar thermal decomposition process with two stages of weight loss. The first weight loss of 4.61% (calcd. 3.97%) for **1**, 3.94% (calcd. 3.95%) for **2**, 4.08% (calcd. 3.97%) for **3**, and 4.91% (calcd. 4.12%) for **4** from 25 to 170 °C is assigned to the liberation of 18 lattice water molecules. The second weight loss of 7.94% (calcd. 7.98%) for **1**, 8.53% (calcd. 7.96%) for **2**, 8.65% (calcd. 7.99%) for **3**, and 8.15% (calcd. 8.30%) for **4** occurs in the temperature region of 170−800 °C, which can be attributed to the release of eight CH_3^+ group together with four O atoms,[33] the dehydration of 12 protons and the removal of eight dimethylamine groups. The result of the TG analysis basically agrees with that of the structure determination of **1**−**4**. To further explore their thermal decomposition procedure, temperature-dependent PXRD patterns, temperature-dependent IR spectra, and temperature-dependent photoluminescence emission spectra of **1** as a representative were thoroughly studied at the temperatures of 25, 100, 200, 400, 600, and 750 °C, selected according to the TG curve of **1**. Furthermore, the color changes of **1** at different temperatures were also recorded (Figure 4a). As the temperature rises from 25 to 200 °C, the

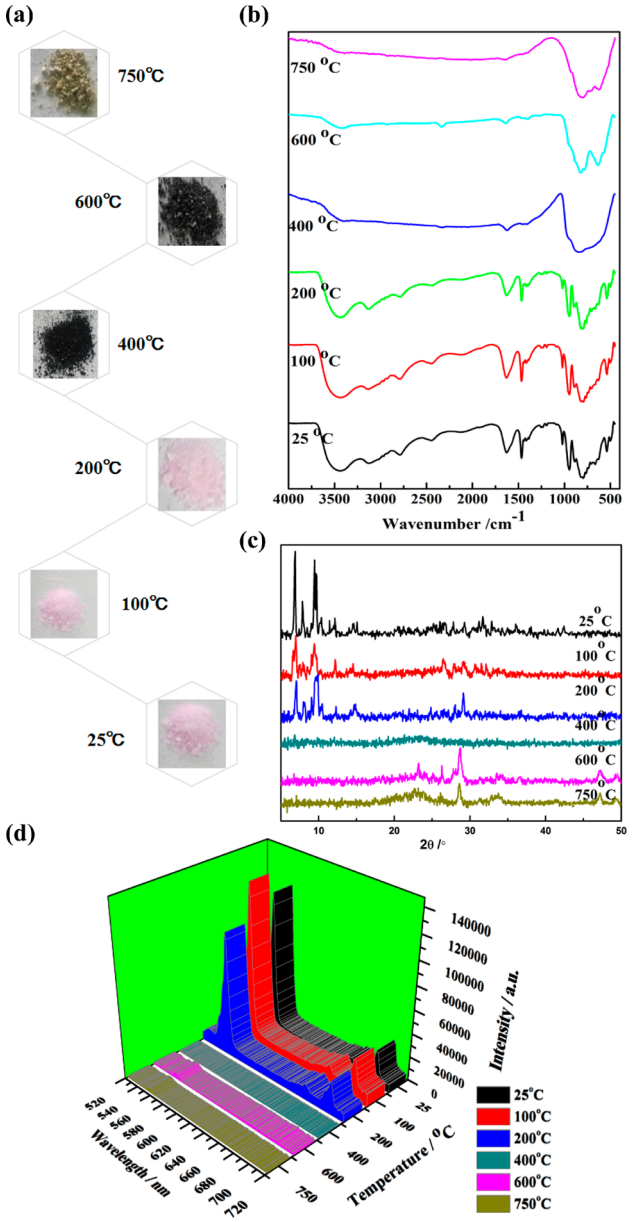

Figure 4. (a) Colors of **1** at different temperatures. (b) Evolution of IR spectra of **1** at different temperatures. (c) Evolution of PXRD patterns of **1** at different temperatures. (d) Evolution of fluorescence emission spectra of **1** at different temperatures.

characteristic vibration bands in IR spectra (Figure 4b) and the characteristic diffraction peaks in PXRD patterns (Figure 4c) are almost unchanged, demonstrating that the backbone of **1** is relatively stable during this temperature range although some lattice water molecules are removed away. (Notably, some slight changes in the PXRD patterns upon heating to 100 and 200 °C are due to the loss of lattice water molecules.) Besides, the fluorescence emission spectra of **1** remain almost unchanged from 25 to 200 °C (Figure 4d), which is in excellent agreement with the results of TG analysis, PXRD patterns and IR spectra. From Figure 4a, when the temperature increases from 200 to 400 °C, we can intuitively see that **1** turns from pink crystals into amorphous black powders, the reason for which may be on account of the loss of lattice water molecules and the carbonization of organic components. At 400 °C, the characteristic vibration peaks of $\nu(W{-}O_t)$, $\nu(W{-}$

DOI: 10.1021/acs.inorgchem.8b01486
Inorg. Chem. 2018, 57, 12509−12520

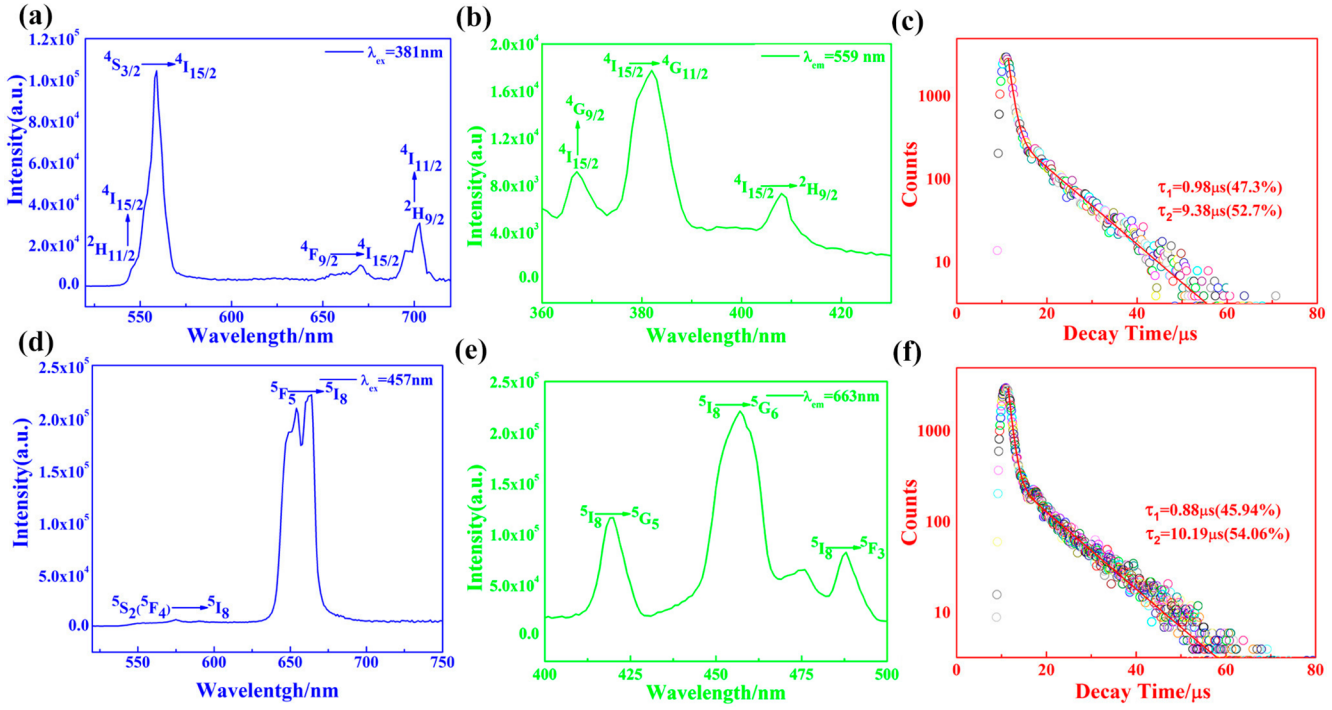

Figure 5. (a) Visible emission spectrum of **1** under the excitation at 381 nm at room temperature. (b) Excitation spectrum of **1** obtained by monitoring the emission at 559 nm at room temperature. (c) Decay curve of **1** under monitoring the excitation at 381 nm and the emission at 559 nm. (d) Visible emission spectrum of **3** under the excitation at 457 nm at room temperature. (e) Excitation spectrum of **3** obtained by monitoring the emission at 663 nm at room temperature. (f) Decay curve of **3** under monitoring the excitation at 457 nm and the emission at 663 nm.

O_b), ν(W−O_c), and ν(Te−O_a) of $[B\text{-}\beta\text{-}TeW_7O_{28}]^{10-}$ fragments in the IR spectrum of **1** gradually vanish. Moreover, the N−H and C−H stretching vibrations in the IR spectrum are unseen, which further confirms that organic components have been indeed carbonized. Correspondingly, some diffraction peaks in the small 2θ region in the PXRD patterns of **1** have disappeared, evidencing the polyoxoanion decomposition of **1**. At the same time, the strongest fluorescent emission peaks are invisible, which results from the case that carbonized black powders of **1** cannot emit the fluorescence. When the temperature is elevated from 400 to 600 °C, the characteristic diffraction peaks derived from the polyoxoanion skeleton in the small 2θ region have totally died away, and the occurrence of some new diffraction peaks in the range of 20−30° manifests that a new phase comes to appear, which may be in relation to the collapse of the polyoxoanion framework. As the temperature continuously increases to 750 °C, new diffraction peaks form in the PXRD pattern, and the intensity of these peaks is also strengthened, declaring that the process of generating new phases has finished. Correspondingly, at 600 °C, the fluorescent emission peak intensity slightly increases, however, at 750 °C, the fluorescent emission peaks disappear, which further consolidates that the process of generating new phases has completed.

Photoluminescence (PL) Properties. In 1937, Vleck wrote a meaningful article entitled "The Puzzle of Rare-Earth Spectra in Solids" that perfectly mirrored the fascination of the intricate optical properties of the trivalent RE ions.[34] As is well-known, RE ions are characterized by a gradual filling of the 4f orbitals from $4f^0$ to $4f^{14}$. These electronic $[Xe]4f^n$ configurations can lead to various electron energy levels which are great shielded by the outer filled 5s and 5p subshells. As a result, except for La^{3+} and Lu^{3+}, each RE^{3+} ion shows different characteristic emissions derived from intra 4f−4f transitions. Thereby, the solid-state visible PL properties of **1** and **3** have been investigated at room temperature. When **1** was excited under an ultraviolet light of 381 nm, the emission spectrum was collected with four characteristic luminescent emission bands with maxima at 545, 559, 670, and 703 nm (Figure 5a), which are respectively attributed to $^2H_{11/2} \rightarrow {}^4I_{15/2}$, $^4S_{3/2} \rightarrow {}^4I_{15/2}$, $^4F_{9/2} \rightarrow {}^4I_{15/2}$, and $^2H_{9/2} \rightarrow {}^4I_{11/2}$ transitions of the Er^{3+} ions.[35] Obviously, the $^4S_{3/2} \rightarrow {}^4I_{15/2}$ emission at 559 nm indicates that **1** exhibits yellowish green luminescence. Concurrently, the excitation spectrum was also collected and shows three characteristic excitation bands at 367, 381, and 408 nm (Figure 5b), which are respectively ascribed to $^4I_{15/2} \rightarrow {}^4G_{9/2}$, $^4I_{15/2} \rightarrow {}^4G_{11/2}$, and $^4I_{15/2} \rightarrow {}^2H_{9/2}$ transitions of the Er^{3+} ions. In order to further determine the decay lifetime, the luminescence decay curve of **1** has been performed for monitoring the emission at 559 nm, which can be fitted to the second-order exponential function with the formula $I = A_1\exp(t/\tau_1) + A_2\exp(t/\tau_2)$. τ_1 and τ_2 are the fast and slow components of the luminescence lifetimes, and A_1 and A_2 are the pre-exponential factors. The fitting luminescence lifetimes τ_1 and τ_2 are 0.98 μs (47.3%) and 9.38 μs (52.7%), and the pre-exponential factors A_1 and A_2 are 3097.98 and 360.43 (Figure 5c, Table S3). Therefore, the average decay time (τ^*) can be calculated with the following equation $\tau^* = (A_1\tau_1^2 + A_2\tau_2^2)/(A_1\tau_1 + A_2\tau_2)$,[36] which is determined to be 5.41 μs. The solid-state sample of **3** emits the orange luminescence under the excitation at 457 nm. The emission spectrum between 520 and 750 nm displays two characteristic emission bands at 575 and 663 nm (Figure 5d) attributed to the $^5S_2(^5F_4) \rightarrow {}^5I_8$ and $^5F_5 \rightarrow {}^5I_8$ transitions of the Ho^{3+} ions, respectively.[37] The excitation spectrum of **3** obtained by monitoring the emission at 663 nm consists of three characteristic excitation peaks at

DOI: 10.1021/acs.inorgchem.8b01486
Inorg. Chem. 2018, 57, 12509−12520

420, 457, and 488 nm (Figure 5e), which are assigned to the transitions of $^5I_8 \rightarrow {}^5G_5$, $^5I_8 \rightarrow {}^5G_6$, and $^5I_8 \rightarrow {}^5F_3$ of the Ho^{3+} ions, respectively. The decay time curve of **3** on monitoring the emission at 663 nm conforms to a second-order exponential function, thus leading to τ_1 = 0.88 μs (45.94%), τ_2 = 10.19 μs (54.06%), and the pre-exponential factors A_1 = 2988.03, A_2 = 303.69, and τ^* = 6.03 μs (Figure 5f, Table S3). To further investigate whether inorganic $[B\text{-}\alpha\text{-}TeW_7O_{28}]^{10-}$ and $[W_5O_{18}]^{6-}$ fragments and dimethyltin cations make the contribution or not during the course of visible emission of **1** and **3**, the emission spectra of **4**, which has no RE-centered luminescence for their empty 4f shell, have been detected under the same conditions as those for **1** and **3** (Figure S9). Also, the visible emission spectra of $Sn(CH_3)_2Cl_2$ have been collected under the same conditions as those for **1** and **3** (Figure S10). We can clearly see from Figure S9 that there is no obvious band appearing in the emission spectra, which can manifest no contribution of the O → W LMCT derived from $[B\text{-}\alpha\text{-}TeW_7O_{28}]^{10-}$ and $[W_5O_{18}]^{6-}$ fragments in the characteristic emission bands of **1** and **3** in the visible region. As shown in Figure S10, there is no apparent contribution from dimethyltin cations in the characteristic emission bands of **1** and **3** in the visible region. As a result, the PL emission properties of **1** and **3** in the visible region mainly stem from the f−f transitions of RE cations. In addition, the temperature-dependent PL emission spectra of **3** in the visible region were measured in the range of 80−300 K (Figure 6). It can be observed that the PL emission intensities of **3** gradually decrease with elevating temperature because of thermal quenching effect.[38]

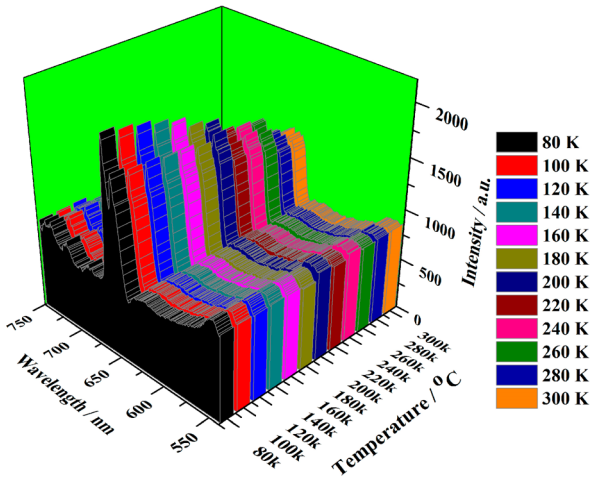

Figure 6. PL emission spectra of **3** with various temperatures.

Recently, RE-based near-infrared (NIR) luminescence materials have attracted significant interest in account of extensive applications in the fields of light emitting diodes, telecommunication as well as medical science due to their potential for noninvasive in biovivo imaging.[39] Herein, the solid-state NIR PL properties of **1** and **3** have been measured at room temperature. When the solid-state sample of **1** was excited under UV light of 381 nm, the NIR emission spectrum of **1** was obtained revealing only one characteristic emission peak at 1531 nm, which can be assigned to the $^4I_{13/2} \rightarrow {}^4I_{15/2}$ transition of the Er^{3+} ions (Figure 7a).[40] The excitation spectrum shows three characteristic excitation bands with maxima at 369, 385, and 412 nm, which are respectively attributed to $^4I_{15/2} \rightarrow {}^4G_{9/2}$, $^4I_{15/2} \rightarrow {}^4G_{11/2}$, and $^4I_{15/2} \rightarrow {}^2H_{9/2}$ transitions of the Er^{3+} ions (Figure 7b). Furthermore, the luminescent decay curve was also collected for monitoring the emission at 1531 nm and conforms to a second-order exponential function. The fitting luminescence lifetimes τ_1 and τ_2 are 1.25 μs (29.21%) and 8.00 μs (70.79%), and the pre-exponential factors A_1 and A_2 are 1419.11 and 538.01 (Figure 7c, Table S4). The average lifetime is calculated to be 6.03 μs. Upon the excitation at 457 nm, the NIR emission spectrum of **3** shows a sharp peak at 983 nm assigned to the $^5F_5 \rightarrow {}^5I_6$ transition of the Ho^{3+} ions (Figure 7d). The excitation spectrum of **3** obtained by monitoring the emission at 983 nm consists of three characteristic excitation peaks at 418, 454, and 485 nm (Figure 7e) resulting from the $^5I_8 \rightarrow {}^5G_5$, $^5I_8 \rightarrow {}^5G_6$, and $^5I_8 \rightarrow {}^5F_3$ transitions of the Ho^{3+} ions, respectively.[35] The luminescent decay curve upon monitoring the emission of 983 nm adheres to a second-order exponential function. The resulting values τ_1 = 0.79 μs (33.92%), τ_2 = 9.92 μs (66.08%), and the pre-exponential factors A_1 = 1822.20, A_2 = 281.48, and τ^* = 6.82 μs were obtained (Figure 7f, Table S4). Similarly, the solid-state NIR emission spectra of **4** and $Sn(CH_3)_2Cl_2$ have been examined under the same conditions as those for **1** and **3** (Figures S11 and S12). The results indicate that there is no evident PL emission contribution from the O → W LMCT of $[B\text{-}\alpha\text{-}TeW_7O_{28}]^{10-}$ and $[W_5O_{18}]^{6-}$ fragments and no evident contribution derived from dimethyltin cations in the characteristic emission bands of **1** and **3** in the NIR region.

In addition, the time-resolved emission spectra (TRES) of **1** were measured in the emission wavelength range of 520−720 nm with an interval of 1.9 nm under the excitation at 381 nm and sliced between 10.4 and 29.6 μs, which provides some meaningful information to study the PL dynamics and energy transfer of **1**. From Figure 8a, we can see that the intensity of the four characteristic emission peaks of Er^{III} ions reaches maximum at a decay time of 10.7 μs and then descends consecutively over time until 29.6 μs. Besides, in the range of 10−22 μs, the emission intensity of the broad band at 559 nm decreases gradually (Figure S13). The emission spectral shapes and the relative intensities of four characteristic emission peaks are not obviously changeable in the time range of 10.4 and 29.6 μs, illustrating that no obvious energy transfer between TT fragments or dimethyltin groups and Er^{3+} ions occurs in the emission process of **1**. Therefore, we can assign the lifetime contributions of two types of crystallographically unique Er^{3+} cations during the PL emission process of **1**. In **1**, the $Er1^{3+}$ cation is situated in an eight-coordinate bicapped trigonal prism constituted by two μ_2-O atoms, two μ_3-O atoms, and one μ_6-O atom from the $[W_5O_{18}]^{6-}$ subunit as well as three μ_3-O atoms from the $[B\text{-}\alpha\text{-}TeW_7O_{28}]^{10-}$ subunit, whereas the $Er2^{3+}$ cation inhabits an eight-coordinate square antiprism defined by two μ_2-O atoms and one μ_4-O atom from one $[B\text{-}\alpha\text{-}TeW_7O_{28}]^{10-}$ subunit and two μ_2-OH groups, one μ_4-O, and two μ_2-O atoms from the other $[B\text{-}\alpha\text{-}TeW_7O_{28}]^{10-}$ subunit. As is well-known, the hydroxyl groups in connection with RE cations can lead to the luminescence quenching and shorten the decay lifetime by the high-frequency O−H oscillators.[41] As for **1**, the short lifetime τ_1 (0.98 μs) with the contribution (47.31%) may mainly result from the square antiprismatic $Er2^{3+}$ cation because each $Er2^{3+}$ cation is combined with two OH^- groups, while the long lifetime τ_2 (9.38 μs) with the contribution (52.7%) may mostly stem from the bicapped trigonal prismatic $Er1^{3+}$ cation without OH^- groups. The

DOI: 10.1021/acs.inorgchem.8b01486
Inorg. Chem. 2018, 57, 12509−12520

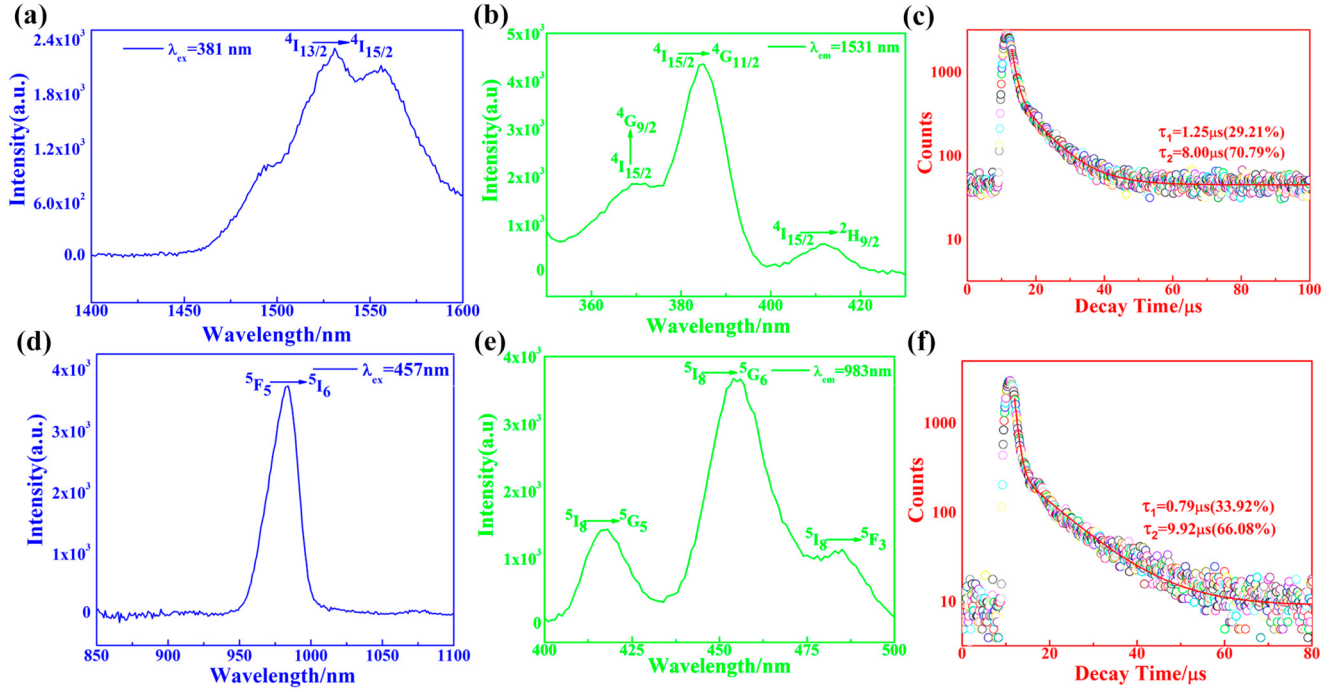

Figure 7. (a) NIR emission spectrum of **1** under the excitation at 381 nm at room temperature. (b) Excitation spectrum of **1** obtained by monitoring the emission at 1531 nm at room temperature. (c) Lifetime decay curve of **1** under monitoring the excitation at 381 nm and the emission at 1531 nm. (d) NIR emission spectrum of **3** under the excitation at 457 nm at room temperature. (e) Excitation spectrum of **3** obtained by monitoring the emission at 983 nm at room temperature. (f) Lifetime decay curve of **3** under monitoring the excitation at 457 nm and the emission at 983 nm.

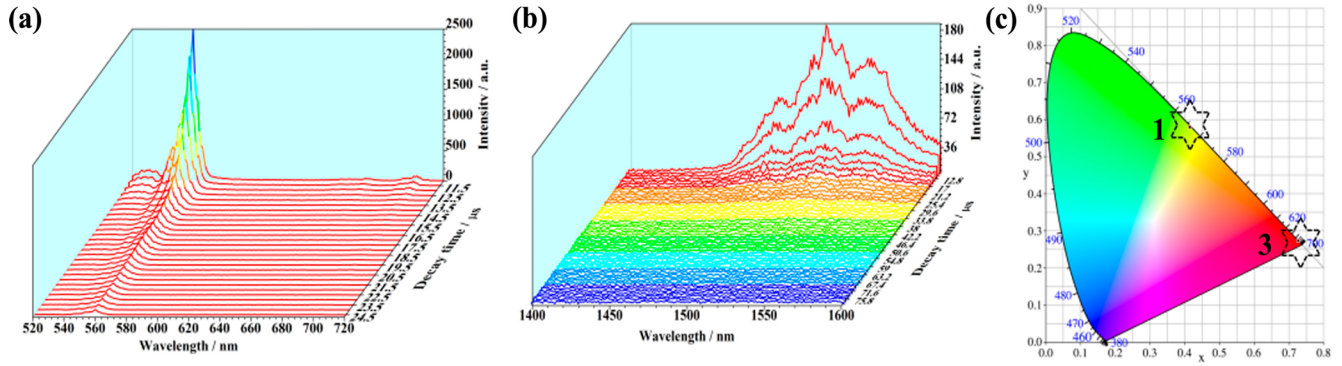

Figure 8. (a) TRES of **1** in the visible region. (b) TRES of **1** in the NIR region. (c) CIE 1931 diagram of **1** and **3**.

TRES presented in Figure 8b shows one characteristic emission band of the Er^{3+} ions, and the emission spectral shapes and the relative intensities remain essentially unchanged apart from a steady decrease in intensity in the successive decay time range of 10−50 μs. This observation illustrates the lack of intermolecular O → W LMCT or dimethyltin groups sensitizing the luminescence of Er^{3+} cations during the emission course of **1** in the range of the NIR region. As no energy transfer contribution of TTs or dimethyltin groups was checked for **1**, it can be deduced that two decay lifetimes result from two crystallographic unique Er^{3+} centers.

The CIE 1931 (Commission International d'Eclairage) diagram has been broadly applied to estimate all possible colors by the combination of three primary colors offering a pervasive method to acquire a good knowledge of the trueness of color for their applications in lighting-emitting devices and is particularly suitable for quantifying the tunability of the emission wavelength as well as the altering of the emission intensity. Herein, the CIE chromaticity coordinates for **1** and **3** determined on the basis of their corresponding PL spectra are indexed to be (0.41413, 0.58004) and (0.72617, 0.27377), which display that **1** and **3** respectively emit yellowish green and orange red in the visible region (Figure 8c).

Various RE co-doped materials have attracted increasing interest because of potential applications in the fields such as solar cells, optical amplifiers, three-dimensional displays, photocatalysis, and biomedicine.[42] In this respect, especially, energy transfer between different RE centers plays a predominant role in tunable luminescence by manipulating the population of excited states of the co-doped RE ions. In this field, Yb^{3+}/Er^{3+} co-doped materials have received intense attention because the Yb^{3+} ion can act as an ideal sensitizer in efficiently transferring absorbed energy to the Er^{3+} ion;[43] meanwhile, the Er^{3+} ion has excited states similar to those of the Yb^{3+} ion. Therefore, we varied the doping mass ratio of $Er(NO_3)_3{\cdot}6H_2O$ (Er)/$Yb(NO_3)_3{\cdot}6H_2O$ (Yb) (The mass ratio

DOI: 10.1021/acs.inorgchem.8b01486
Inorg. Chem. 2018, 57, 12509−12520

of Er/Yb is in the range of 0.02:0.98−0.96:0.04) and obtained various **1-Er/Yb** co-doped samples. Under the excitation at 381 nm, the solid-state emission spectra of various **1-Er/Yb** co-doped samples in the visible and NIR regions have been collected at room temperature. As shown in Figure 9a, the addition of the Yb^{3+} ion has no influence on the positions of four characteristic emission bands resulting from $^2H_{11/2} \rightarrow {}^4I_{15/2}$, $^4S_{3/2} \rightarrow {}^4I_{15/2}$, $^4F_{9/2} \rightarrow {}^4I_{15/2}$, and $^2H_{9/2} \rightarrow {}^4I_{11/2}$ transitions of the Er^{3+} ions. The strongest emission peak is also observed at ca. 558 nm, yet the intensities of emission bands varies with the increase of Yb^{3+} concentration. It is interesting that the intensities of the emission peaks of **1-Er/Yb** co-doped samples gradually increase with different mass ratio of Er/Yb in the range of 0.96:0.04−0.40:0.60 in the synthetic procedure, whereas the intensities of the emission peaks of **1-Er/Yb** co-doped samples decrease when the mass ratio of Er/Yb increases from 0.40:0.60 and 0.02:0.98. Obviously, the emission intensity reaches the maximum at the mass ratio of Er/Yb being 0.40:0.60. At the same time, the evolution of the intensity of the emission peak at 558 nm of various **1-Er/Yb** co-doped samples is illustrated in Figure 9b, indicating that the intensity of the emission peak first increases and then decreases with the increase of Yb^{3+} co-doping concentration, which is analogous to the previous report addressed by Dong's group.[43] The main reason for this trend can be explained by the fact that with increasing the Yb^{3+} co-doping concentration, more Yb^{3+} sensitizers become available to be excited and transfer more energy to the Er^{3+} activators so that the intensity of the emission increases. Subsequently, continuing to increase of Yb^{3+} concentration can lead to energy transfer from the excitation of Er^{3+} ions back to Yb^{3+} ions due to the fact that the $^2F_{5/2}$ of Yb and $^4I_{11/2}$ of Er have similar energy values;[44] besides, the decrease of Er^{3+} concentration also contributes to the decrease of the intensity. Moreover, for the purpose of investigating their lifetimes, the PL decay curves are recorded upon monitoring the excitation at 381 nm and the emission at 556 nm (Figure 10a) and conform to the biexponential function. The related lifetime values are represented in Table S5. Figure 10b displays the average decay time (τ^*) evolution of various **1-Er/Yb** co-doped samples in the visible region with decreasing the mass ratio of Er/Yb, from which it can be clearly seen that the average decay time (5.70 μs) is most maximal when the mass ratio of Er/Yb is 0.40:0.60, which further consolidates energy transfer from the Yb^{3+} sensitizers to the Er^{3+} activators during the course of emission of various **1-Er/Yb** co-doped samples. As shown in Figure 9c, all the NIR emission spectra of various **1-Er/Yb** co-doped samples show an emission peak at 1532 nm derived from the $^4I_{13/2} \rightarrow {}^4I_{15/2}$ transition of the Er^{3+} ions. Apparently, the emission intensity monotonically decreases with the addition of the Yb^{3+} ions. No maximum value in the emission intensity in the NIR region is observed with the addition of the Yb^{3+} ions, which suggests that the Yb^{3+} ions cannot effectively transfer energy to sensitize the emission of the Er^{3+} ions in the NIR region. The major reason why the emission intensity generally decreases with the addition of the Yb^{3+} ions is that the decline of the percentage of the Er^{3+} ions in various **1-Er/Yb** co-doped samples leads to the weakness of the emission intensity. The obvious descending trend of the intensity of the emission peak at 1532 nm with increasing the Yb^{3+} concentration (Figure 9d) also implies the fast depopulation of the $^4I_{13/2}$ manifold, which is in accordance with the previous literature.[45] Likewise, the decay curves of various **1-Er/Yb** co-doped samples are also recorded by monitoring the excitation at 381 nm and the emission at 1531 nm (Figure 10c) and are well-fitted the biexponential function and relevant fitting data are exhibited in Table S6 as well. Figure 10d exhibits the average decay time (τ^*) change of various **1-Er/Yb** co-doped samples in NIR region with decreasing the mass ratio of Er/Yb.

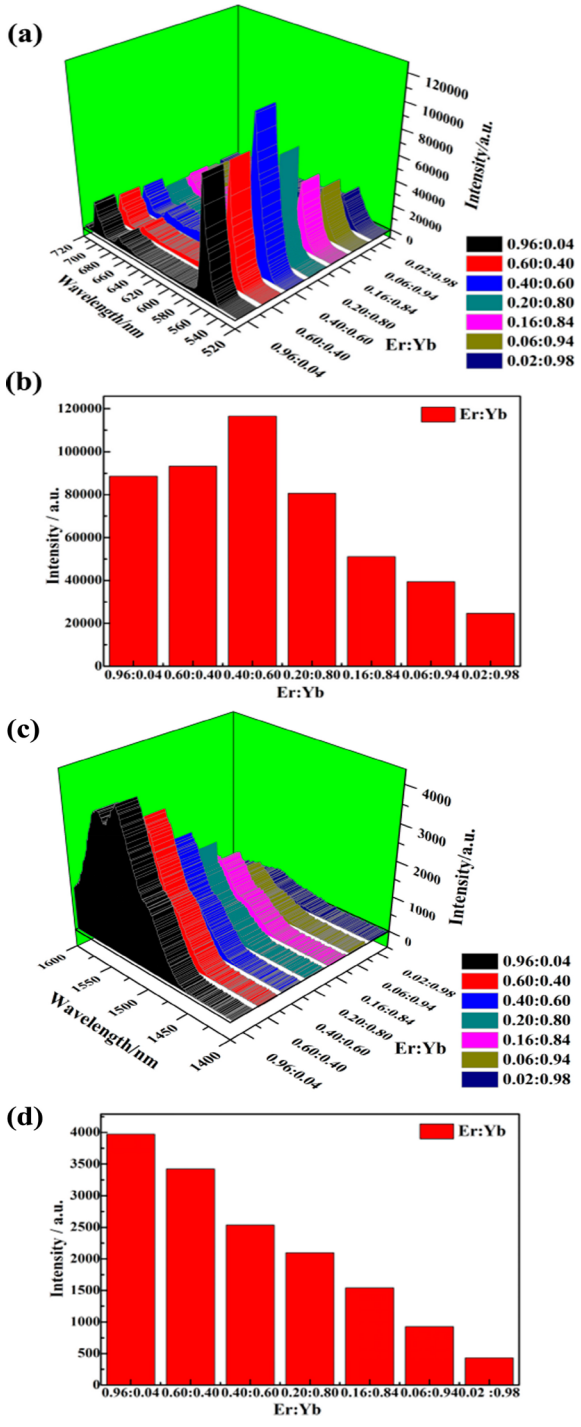

Figure 9. (a) Solid-state visible emission spectral evolution of various **1-Er/Yb** co-doped samples under the excitation at 381 nm. (b) Evolution of the intensity of the emission peak at 558 nm of various **1-Er/Yb** co-doped samples. (c) Solid-state NIR emission spectral evolution of various **1-Er/Yb** co-doped samples under the excitation at 381 nm. (d) Evolution of the intensity of the emission peak at 1532 nm of various **1-Er/Yb** co-doped samples.

DOI: 10.1021/acs.inorgchem.8b01486
Inorg. Chem. 2018, 57, 12509−12520

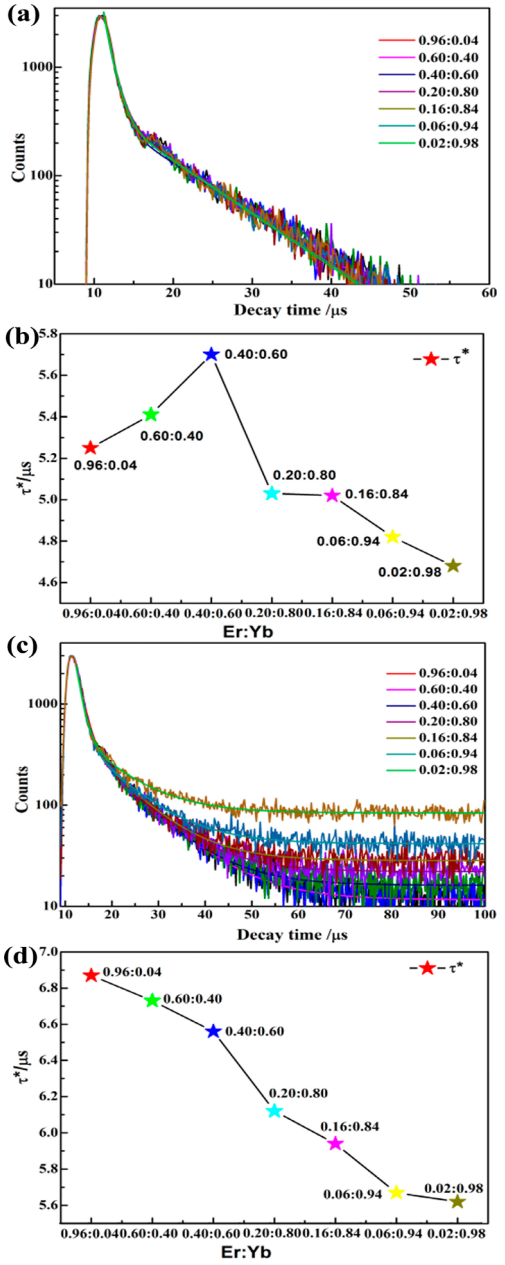

Figure 10. (a) PL decay curves of various **1-Er/Yb** co-doped samples recorded upon monitoring the excitation at 381 nm and the emission at 556 nm. (b) Average decay time evolution of various **1-Er/Yb** co-doped samples in visible region with decreasing the mass ratio of Er/Yb. (c) PL decay curves of various **1-Er/Yb** co-doped samples recorded upon monitoring the excitation at 381 nm and the emission at 1531 nm. (d) Average decay time evolution of various **1-Er/Yb** co-doped samples in NIR region with decreasing the mass ratio of Er/Yb.

It can be evidently observed that the average decay times gradually become short with the addition of the Yb^{3+} ions, which further manifest that no energy transfer from the Yb^{3+} ions to the Er^{3+} ions occurs in the NIR emission procedure. From the above-mentioned analysis, it can be concluded that for **1-Er/Yb** co-doped samples the Yb^{3+} ions can sensitize the Er^{3+} ions to enhance the emission intensity in the visible region whereas the Yb^{3+} ions cannot sensitize the Er^{3+} ions to improve the emission intensity in the NIR region.

It is well-known that Er/Yb co-doped materials with low phonon frequencies and high chemical stability are able to convert near-infrared long-wavelength excitation radiation into shorter visible wavelength radiation through photon upconversion (UC) processes, which offers advantages such as low autofluorescence background and large anti-Stokes shifts.[46] In order to explore whether various **1-Er/Yb** co-doped samples have the special UC emission behavior, we investigated the dependent plot of the UC emission intensity versus concentration under the excitation at 980 nm at room temperature. It can be seen from Figure S14 that there is an extremely weak green emission band at 531 nm derived from the $^2H_{11/2} \rightarrow {}^4I_{15/2}$ transition with a shoulder emission band at 554 nm attributed to the $^4S_{3/2} \rightarrow {}^4I_{15/2}$ transition increasing gently when the mass ratio of Er/Yb varies in the range of 0.96:0.04−0.16:0.84. Suddenly, the intensities of the emission bands increase dramatically when the mass ratio of Er/Yb reaches 0.06:0.94 (Figure 11a). Upon further decreasing the

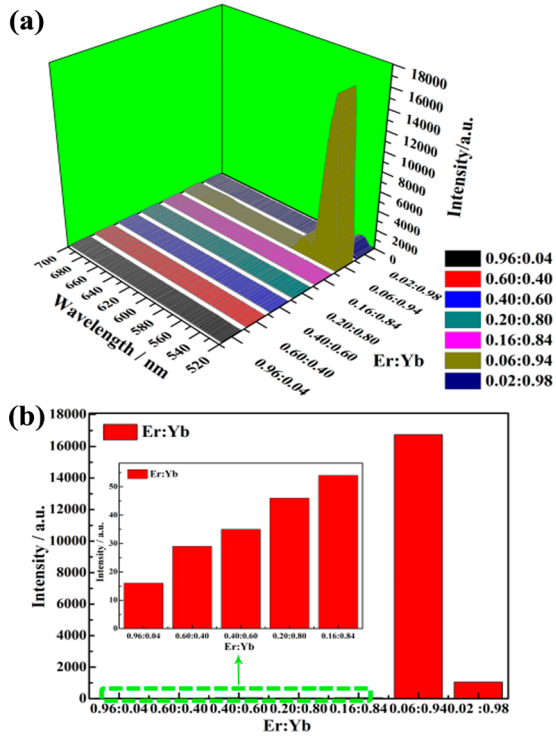

Figure 11. (a) UC emission spectra of various **1-Er/Yb** co-doped samples under excitation at 980 nm. (b) Evolution of the intensity of the emission peak at 531 nm of various **1-Er/Yb** co-doped samples. Inset shows the evolution of the intensity of the emission peak at 531 nm with mass ratio of Er/Yb in the range of 0.96:0.04−0.16:0.84.

mass ratio of Er/Yb, the intensities of the emission bands greatly decline. From Figure 11b, we can see that the upconversion emission reaches a summit at the mass ratio of 0.06:0.94 with the continuing increase of the Yb^{3+} ions. The phenomenon that the emission intensity first increases and then decreases with the increase of Yb^{3+} co-doping concentration could be attributed to the cross relaxation.[47,48] When the doping concentration of Yb^{3+} is low, the intensity is gradually increasing but can hardly be observed in Figure 11b due to the fact that weak cross relaxation has slightly influence on the UC process. When the mass ratio of Er/Yb reaches 0.06:0.94, the strong cross-relaxation within the dopants leading to the appearance of the strongest intensity; however, the high concentration of Yb^{3+} will inevitably evoke serious

DOI: 10.1021/acs.inorgchem.8b01486
Inorg. Chem. 2018, 57, 12509−12520

concentration quenching resulting in a low UC emission intensity.[47,48] To the best of our knowledge, this single-band UC green emission (Figure 11a) is relatively rare and is for the first time observed in POMs in comparison with the UC double-band emissions of Er^{3+} ions containing green ($^2H_{11/2}/^4S_{3/2} \rightarrow {}^4I_{15/2}$) and red ($^4F_{9/2} \rightarrow {}^4I_{15/2}$) wavelengths.[49]

CONCLUSION

In conclusion, by the one-pot synthetic strategy of mixing sodium tungstate, potassium tellurite, $RE(NO_3)_3{\cdot}6H_2O$, dimethyltin dichloride, and dimethylamine hydrochloride in aqueous solution at room temperature, a class of dimethyltin-functionalized RE-incorporated TTs $[H_2N(CH_3)_2]_8Na_4H_2[RE_2(OH)(B\text{-}\alpha\text{-}TeW_7O_{28})\text{-}Sn_2(CH_3)_4(W_5O_{18})]_2{\cdot}18H_2O$ [RE = Er^{III} (**1**), Yb^{III} (**2**), Ho^{III} (**3**), Y^{III} (**4**)] have been obtained, and they contain two pentavacant Keggin $[B\text{-}\alpha\text{-}TeW_7O_{28}]^{12-}$ and two monovacant Lindqvist $[W_5O_{18}]^{6-}$ fragments connected by RE and dimethyltin linkers. Furthermore, various **1-Er/Yb** co-doped samples were first prepared, and their emission behaviors in the visible and NIR regions were also investigated under the excitation at 381 nm, illustrating that the Yb^{3+} ions can sensitize the Er^{3+} ions to enhance the emission intensity in the visible region rather than in the NIR region. In addition, the UC spectra of various **1-Er/Yb** co-doped samples show a rare single-band green emission at 531 nm and the emission intensity reaches the maximum at the mass ratio of Er/Yb being 0.06:0.94. This work provides a general platform to synthesize organic−inorganic hybrid organometal and RE co-embedded heterometallic POM aggregates and offers some valuable information on deeply pursuing new RE-incorporated POM-based luminescence materials. In following work, we will develop multicolor-tuning POM-based materials in the visible and NIR regions via a multicomponent dopant system.

ASSOCIATED CONTENT

Supporting Information

The Supporting Information is available free of charge on the ACS Publications website at DOI: 10.1021/acs.inorgchem.8b01486.

BVS calculations of RE, Te and W atoms; summary of RE−O bond lengths, RE−O average bond lengths and RE^{III} coordination numbers; related structural figures; TG curves of **1**−**4**; the discussion on IR spectra of **1**−**4**; related luminescence spectra and luminescence decay curves; discussion on magnetic properties of **1** (PDF)

Accession Codes

CCDC 1845942−1845945 contain the supplementary crystallographic data for this paper. These data can be obtained free of charge via www.ccdc.cam.ac.uk/data_request/cif, or by emailing data_request@ccdc.cam.ac.uk, or by contacting The Cambridge Crystallographic Data Centre, 12 Union Road, Cambridge CB2 1EZ, UK; fax: +44 1223 336033.

AUTHOR INFORMATION

Corresponding Authors

*E-mail: ljchen@henu.edu.cn (L.-J. Chen).
*E-mail: zhaojunwei@henu.edu.cn (J.-W. Zhao).

ORCID

Jun-Wei Zhao: 0000-0002-7685-1309

Notes

The authors declare no competing financial interest.

ACKNOWLEDGMENTS

This work was supported by the National Natural Science Foundation of China (21571048, 21671054, 21771052), the Innovation Scientists and Technicians Troop Construction Projects of Henan Province (174100510016), the Program for Science & Technology Innovation Talents in Universities of Henan Province (16HASTIT001), the Foundation of State Key Laboratory of Structural Chemistry (20160016), the 2014 Special Foundation for Scientific Research Project of Henan University (XXJC20140001), and the Students Innovative Pilot Plan of Henan University (16NA005).

REFERENCES

(1) Eliseeva, S. V.; Bünzli, J. -C. G. Lanthanide luminescence for functional materials and bio-science. *Chem. Soc. Rev.* **2010**, *39*, 189−227.

(2) Fang, X.; Kögerler, P.; Furukawa, Y.; Speldrich, M.; Luban, M. Molecular growth of a core−shell polyoxometalate. *Angew. Chem., Int. Ed.* **2011**, *50*, 5212−5216.

(3) Ma, X.; Yang, W.; Chen, L. J.; Zhao, J. W. Significant developments in rare-earth-containing polyoxometalate chemistry: synthetic strategies, structural diversities and correlative properties. *CrystEngComm* **2015**, *17*, 8175−8197.

(4) Wang, S.-S.; Yang, G.-Y. Recent advances in polyoxometalate -catalyzed reactions. *Chem. Rev.* **2015**, *115*, 4893−4962.

(5) Liu, J.-C.; Han, Q.; Chen, L.-J.; Zhao, J.-W.; Streb, C.; Song, Y.-F. Aggregation of giant cerium−bismuth tungstate clusters into a 3D porous framework with gigh proton conductivity. *Angew. Chem., Int. Ed.* **2018**, *57*, 8416−8420.

(6) Zhao, J.-W.; Li, Y.-Z.; Chen, L.-J.; Yang, G.-Y. Research progress on polyoxometalate-based transition-metal−rare-earth heterometallic derived materials: synthetic strategie. *Chem. Commun.* **2016**, *52*, 4418−4445.

(7) Ismail, A. H.; Nsouli, N. H.; Dickman, M. H.; Knez, J.; Kortz, U. The 20-tungsto-4-tellurate(IV) $[H_2Te_4W_{20}O_{80}]^{22-}$ and the 15-tungstotellurate(IV) $[NaTeW_{15}O_{54}]^{13-}$. *J. Cluster Sci.* **2009**, *20*, 453−465.

(8) Gaunt, A. J.; May, I.; Copping, R.; Bhatt, A. I.; Collison, D.; Fox, O. D.; Holman, K. T.; Pope, M. T. A new structural family of heteropolytungstate lacunary complexes with the uranyl, UO_2^{2+}, cation. *Dalton Trans.* **2003**, 3009−3014.

(9) Gao, J.; Yan, J.; Mitchell, S. G.; Miras, H. N.; Boulay, A. G.; Long, D.-L.; Cronin, L. Self-assembly of a family of macrocyclic polyoxotungstates with emergent material properties. *Chem. Sci.* **2011**, *2*, 1502−1508.

(10) Bösing, M.; Nöh, A.; Loose, I.; Krebs, B. Highly efficient catalysts in directed oxygen-transfer processes: synthesis, structures of novel manganese-containing heteropolyanions, and applications in regioselective epoxidation of dienes with hydrogen peroxide. *J. Am. Chem. Soc.* **1998**, *120*, 7252−7259.

(11) Kortz, U.; Savelieff, M. G.; Bassil, B. S.; Keita, B.; Nadjo, L. Synthesis and characterization of iron(III)-substituted, dimeric polyoxotungstates, $[Fe_4(H_2O)_{10}(\beta\text{-}XW_9O_{33})_2]^{n-}$ (n = 6, X = As^{III}, Sb^{III}; n = 4, X = Se^{IV}, Te^{IV}). *Inorg. Chem.* **2002**, *41*, 783−789.

(12) Kalinina, I. V.; Izarova, N. V.; Kortz, U. Bis[tetraruthenium(IV)]- containing polyoxometalates: $[\{Ru^{IV}_4O_6(H_2O)_9\}_2Sb_2W_{20}O_{68}(OH)_2]^{4-}$ and $[\{Ru^{IV}_4O_6(H_2O)_9\}_2\{Fe(H_2O)_2\}_2\{\beta\text{-}TeW_9O_{33}\}_2H]^{-}$. *Inorg. Chem.* **2012**, *51*, 7442−7444.

(13) Zhan, C. H.; Cameron, J. M.; Gao, J.; Purcell, J. W.; Long, D.-L.; Cronin, L. Time-resolved assembly of cluster-in-cluster $\{Ag_{12}\}$-in-$\{W_{76}\}$ polyoxometalates under supramolecular control. *Angew. Chem., Int. Ed.* **2014**, *53*, 10362−10366.

DOI: 10.1021/acs.inorgchem.8b01486
Inorg. Chem. 2018, 57, 12509−12520

(14) Cameron, J. M.; Gao, J.; Long, D.-L.; Cronin, L. Self-assembly and structural transformations of high-nuclearity palladium-rich polyoxometalates. *Inorg. Chem. Front.* **2014**, *1*, 178−185.
(15) Artetxe, B.; Reinoso, S.; San Felices, L. S.; Vitoria, P.; Pache, A.; Martín-Caballero, J.; Gutiérrez-Zorrilla, J. M. Functionalization of Krebs-type polyoxometalates with N,O-chelating ligands: a systematic study. *Inorg. Chem.* **2015**, *54*, 241−252.
(16) Chen, W.-C.; Li, H.-L.; Wang, X.-L.; Shao, K.-Z.; Su, Z.-M.; Wang, E.-B. Assembly of cerium(III)-stabilized polyoxotungstate nanoclusters with SeO_3^{2-}/TeO_3^{2-} templates: from single polyoxoanions to inorganic hollow spheres in dilute solution. *Chem. - Eur. J.* **2013**, *19*, 11007−11015.
(17) Chen, W.-C.; Qin, C.; Wang, X.-L.; Li, Y.-G.; Zang, H.-Y.; Shao, K.-Z.; Su, Z.-M.; Wang, E.-B. Assembly of a large cerium(III)-containing tungstotellurites(IV) nanocluster: $[Ce_{10}Te_8W_{88}O_{298}(OH)_{12}(H_2O)_{40}]^{18-}$. *Dalton Trans.* **2015**, *44*, 11290−11293.
(18) Han, Q.; Wen, Y.; Liu, J.-C.; Zhang, W.; Chen, Li.-J.; Zhao, J.-W. Rare-earth-incorporated tellurotungstate hybrids functionalized by 2-picolinic acid ligands: syntheses, structures, and properties. *Inorg. Chem.* **2017**, *56*, 13228−13240.
(19) Zakharov, V. A.; Yermakov, Yu. I. Supported organometallic catalysts for olefin polymerization. *Catal. Rev.: Sci. Eng.* **1979**, *19*, 67−103.
(20) Long, N. J. Organometallic compounds for nonlinear optics−the search for en-light-enment. *Angew. Chem., Int. Ed. Engl.* **1995**, *34*, 21−38.
(21) Hartinger, C. G.; Dyson, P. J. Bioorganometallic chemistry-from teaching paradigms to medicinal applications. *Chem. Soc. Rev.* **2009**, *38*, 391−401.
(22) Liu, Y. B.; Zhang, Y. H.; Ma, P. T.; Dong, Y. K.; Niu, J. Y.; Wang, J. P. Synthesis, crystal structure and characterization of trivacant-Keggin- polyoxometalate-based carbonyl manganese derivative. *Inorg. Chem. Commun.* **2015**, *56*, 45−47.
(23) Zheng, D.-M.; Wang, R.-Q.; Du, Y.; Hou, G.-F.; Wu, L.-X.; Bi, L.-H. A new organo-ruthenium substituted tungstotellurate: synthesis, structural characterization and catalytic properties. *New J. Chem.* **2016**, *40*, 8829−8836.
(24) Yang, H.; Zhang, L.-C.; Yang, L.; Zhang, X.-L.; You, W.-S.; Zhu, Z.-M. Synthesis, characterization and catalytic activity of a new sandwich-type tungstophosphate functionalized by carboxyethyltin. *Inorg. Chem. Commun.* **2013**, *29*, 33−36.
(25) Han, Q.; Liu, J. C.; Wen, Y.; Chen, L. J.; Zhao, J. W.; Yang, G. Y. Tellurotungstate-based organotin−rare-earth heterometallic hybrids with four organic components. *Inorg. Chem.* **2017**, *56*, 7257−7269.
(26) Li, H. L.; Liu, Y. J.; Zheng, R.; Chen, L. J.; Zhao, J. W.; Yang, G. Y. Trigonal pyramidal {$AsO_2(OH)$} bridging tetranuclear rare-earth encapsulated polyoxotungstate aggregates. *Inorg. Chem.* **2016**, *55*, 3881−3893.
(27) Zhao, J. W.; Li, H. L.; Ma, X.; Xie, Z. G.; Chen, L. J.; Zhu, Y. S. Lanthanide-connecting and lone-electron-pair active trigonal-pyramidal- AsO_3 inducing nanosized poly(polyoxotungstate) aggregates and their snticancer activities. *Sci. Rep.* **2016**, *6*, 26406.
(28) Liu, Y. J.; Li, H. L.; Lu, C. T.; Gong, P. J.; Ma, X. Y.; Chen, L. J.; Zhao, J. W. Organocounterions-assisted and pH-controlled self-assembly of five nanoscale high-nuclear lanthanide substituted heteropolytungstates. *Cryst. Growth Des.* **2017**, *17*, 3917−3928.
(29) Sheldrick, G. M. *SHELXS 97, Program for Crystal Structure Solution*; University of Göttingen: Göttingen, Germany, 1997.
(30) Sheldrick, G. M. *SHELXL 97, Program for Crystal Structure Refinement*; University of Göttingen: Göttingen, Germany, 1997.
(31) Sheldrick, G. M. *SADABS: Program for Absorption Correction*; University of Göttingen: Göttingen, Germany, 1996.
(32) Brown, I. D.; Altermatt, D. Bond-valence parameters obtained from a systematic analysis of the inorganic crystal structure database. *Acta Crystallogr., Sect. B: Struct. Sci.* **1985**, *41*, 244−247.
(33) Reinoso, S.; Dickman, M. H.; Kortz, U. A novel hexatungstate fragment stabilized by dimethyltin groups: $[\{(CH_3)_2Sn\}_2(W_6O_{22})]^{4-}$. *Inorg. Chem.* **2006**, *45*, 10422−10424.
(34) Vleck, J. H. V. The puzzle of rare-earth spectra in solids. *J. Phys. Chem.* **1937**, *41*, 67−80.
(35) Li, H.-L.; Liu, Y.-J.; Liu, J.-L.; Chen, L.-J.; Zhao, J.-W.; Yang, G.-Y. Structural transformation from dimerization to tetramerization of serine-decorated rare-earth-incorporated arsenotungstates induced by the usage of rare-earth salts. *Chem. - Eur. J.* **2017**, *23*, 2673−2689.
(36) Li, P. L.; Wang, Z. J.; Yang, Z. P.; Guo, Q. L. Tunable blue−green emission phosphor Ca_2PO_4Cl:Ce^{3+}, Tb^{3+}: luminescence and energy transfer. *Opt. Commun.* **2014**, *332*, 83−88.
(37) Yu, Z. C.; Zhou, H. F.; Zhou, G. J.; Zhou, J.; Wu, Y. Q.; Zhang, X. S.; Wang, T.; Huang, D. P.; Wang, X. Q.; Hu, J. F. Optical−magnetic bifunctional properties and mechanistic insights on upconversion of NaYF4:Yb, Ho, Tm@NaGdF4 with a tunable nanodumbbell morphology. *Phys. Chem. Chem. Phys.* **2017**, *19*, 31675−31683.
(38) Huo, J. S.; Dong, L. P.; Lü, W.; Shao, B. Q.; You, H. P. Novel tunable green-red-emitting oxynitride phosphors co-activated with Ce^{3+}, Tb^{3+}, and Eu^{3+}: photoluminescence and energy transfer. *Phys. Chem. Chem. Phys.* **2017**, *19*, 17314−17323.
(39) Wang, R.; Li, X. M.; Zhou, L.; Zhang, F. Epitaxial seeded growth of rare-earth nanocrystals with efficient 800 nm near-infrared to 1525 nm short-wavelength infrared downconversion photoluminescence for in vivo bioimaging. *Angew. Chem., Int. Ed.* **2014**, *53*, 12086−12090.
(40) Wawrzynczyk, D.; Piatkowski, D.; Mackowski, S.; Samoc, M.; Nyk, M. Microwave-assisted synthesis and single particle spectroscopy of infrared down- and visible up-conversion in Er^{3+} and Yb^{3+} co-doped fluoride nanowires. *J. Mater. Chem. C* **2015**, *3*, 5332−5338.
(41) Bassett, A. P.; Magennis, S. W.; Glover, P. B.; Lewis, D. J.; Spencer, N.; Parsons, S.; Williams, R. M.; De Cola, L.; Pikramenou, Z. Highly luminescent, triple- and quadruple-stranded, dinuclear Eu, Nd, and Sm(III) lanthanide complexes based on bis-diketonate ligands. *J. Am. Chem. Soc.* **2004**, *126*, 9413−9424.
(42) Zhang, Y. L.; Liu, X. H.; Lang, Y. B.; Yuan, Z.; Zhao, D.; Qin, G. S.; Qin, W. P. Synthesis of ultra-small $BaLuF_5$:Yb^{3+},Er^{3+}@BaLuF5:Yb^{3+} active−core − active−shell nanoparticles with enhanced up-conversion and down-conversion luminescence by a layer-by-layer strategy. *J. Mater. Chem. C* **2015**, *3*, 2045−2053.
(43) Cao, B. S.; He, Y. Y.; Zhang, L.; Dong, B. Upconversion properties of Er^{3+}-Yb^{3+}:$NaYF_4$ phosphors with a wide range of Yb^{3+} concentration. *J. Lumin.* **2013**, *135*, 128−132.
(44) Hinojosa, S.; Meneses-Nava, M. A.; Barbosa-García, O.; Díaz-Torres, L.A.; Santoyo, M. A.; Mosiño, J. F. Energy back transfer, migration and energy transfer (Yb-to-Er and Er-to-Yb) processes in Yb,Er:YAG. *J. Lumin.* **2003**, *102−103*, 694−698.
(45) Xu, D. K.; Liu, C. F.; Yan, J. W.; Yang, S. H.; Zhang, Y. L. Understanding energy transfer mechanisms for tunable emission of Yb^{3+}-Er^{3+} co-doped GdF_3 nanoparticles: concentration-dependent luminescence by near-infrared and violet excitation. *J. Phys. Chem. C* **2015**, *119*, 6852−6860.
(46) Tamilmani, V.; Kumari, A.; Rai, V. K.; Unni Nair, B.; Sreeram, K. J. Bright green frequency upconversion in catechin based Yb^{3+}/Er^{3+} co-doped $LaVO_4$ nanorods upon 980 nm excitation. *J. Phys. Chem. C* **2017**, *121*, 4505−4516.
(47) Wu, M.; Song, E. H.; Chen, Z. T.; Ding, S.; Ye, S.; Zhou, J. J.; Xu, S. Q.; Zhang, Q. Y. Single-band red upconversion luminescence of Yb^{3+}-Er^{3+} via nonequivalent substitution in perovskite $KMgF_3$ nanocrystals. *J. Mater. Chem. C* **2016**, *4*, 1675−1684.
(48) Wei, W.; Zhang, Y.; Chen, R.; Goggi, J. L.; Ren, N.; Huang, L.; Bhakoo, K. K.; Sun, H. D.; Tan, T. T. Y. Cross relaxation induced pure red upconversion in activator- and sensitizer-rich lanthanide nanoparticles. *Chem. Mater.* **2014**, *26*, 5183−5186.
(49) Lei, L.; Zhang, J. J.; Xu, S. Q. The progress of single-band upconversion nanomaterials. *RSC Adv.* **2016**, *6*, 81076−81084.

DOI: 10.1021/acs.inorgchem.8b01486
Inorg. Chem. 2018, 57, 12509−12520